


## Structural and magnetic properties of co-sputtered Fe<sub>0.8</sub>C<sub>0.2</sub> thin films

Prabhat Kumar , V. R. Reddy, V. Ganesan, and Mukul Gupta 

UGC-DAE Consortium for Scientific Research, University Campus, Khandwa Road, Indore 452 001, India

I. Sergueev, O. Leupold , and H.-C. Wille

Deutsches Elektronen-Synchrotron DESY, Notkestrasse 85, D-22607 Hamburg, Germany



(Received 12 July 2019; revised manuscript received 9 December 2019; published 13 January 2020)

We studied the structural and magnetic properties of Fe<sub>0.8</sub>C<sub>0.2</sub> thin films deposited by co-sputtering of Fe and C targets in a direct current magnetron sputtering (dcMS) process at a substrate temperature ( $T_s$ ) of 300, 523, and 773 K. The structure and morphology were measured using x-ray diffraction (XRD), x-ray absorption near-edge spectroscopy (XANES) at Fe  $L$  and C  $K$  edges and atomic/magnetic force microscopy (AFM, MFM). An ultrathin (3-nm) <sup>57</sup>Fe<sub>0.8</sub>C<sub>0.2</sub> layer, placed between relatively thick Fe<sub>0.8</sub>C<sub>0.2</sub> layers was used to estimate Fe self-diffusion taking place during growth at different  $T_s$  using depth profiling measurements. Such <sup>57</sup>Fe<sub>0.8</sub>C<sub>0.2</sub> layer was also used for <sup>57</sup>Fe conversion electron Mössbauer spectroscopy (CEMS) and nuclear resonance scattering (NRS) measurements, yielding the magnetic structure of this ultrathin layer. We found from XRD measurements that the structure formed at low  $T_s$  (300 K) is analogous to Fe-based amorphous alloy and at high  $T_s$  (773 K), predominantly a Fe<sub>3</sub>C phase has been formed. Interestingly, at an intermediate  $T_s$  (523 K), a clear presence of Fe<sub>4</sub>C (along with Fe<sub>3</sub>C and Fe) can be seen from the NRS spectra. The microstructure obtained from AFM images was found to be in agreement with XRD results. MFM results also agree well with NRS as the presence of multi-magnetic components can be clearly seen in the sample grown at  $T_s = 523$  K. The information about the hybridization between Fe and C, obtained from Fe  $L$ - and C  $K$ -edge XANES also supports the results obtained from other measurements. In essence, from this work, a possibility for experimental realization of Fe<sub>4</sub>C has been demonstrated. It can be anticipated that by further fine-tuning of the deposition conditions, even single-phase Fe<sub>4</sub>C can be realized which hitherto remains an experimental challenge.

DOI: 10.1103/PhysRevMaterials.4.013402

### I. INTRODUCTION

Tetra iron compounds (Fe<sub>4</sub>X) are an interesting class of compound known to exhibit higher (than Fe) magnetic moment ( $M$ ) [1–4] and spin-polarization ratio (SPR) [5,6]. In addition, metallic resistivity and corrosion resistance of Fe<sub>4</sub>X make them attractive for applications. The structure of Fe<sub>4</sub>X compounds have been classified as antiperovskite [ $P = \bar{4}3m(215)$ ] and metalloid element such as  $X = B, C, N$  occupy the body center position within the face center cubic (fcc) lattice of host Fe. Theoretically, predicted values of  $M$  for Fe<sub>4</sub>B, Fe<sub>4</sub>C, and Fe<sub>4</sub>N are 2.57, 2.42, and 2.62  $\mu_B$  [1–4,6], respectively. Such an enhancement in  $M$  occurs due to the volume expansion of Fe lattice. An expansion in volume produces a higher density of states near the Fermi level due to contraction of  $d$  band (relative to Fe) and therefore results in higher  $M$ . The increase in  $M$  due to volume expansion is known as magnetovolume effect [7]. Experimentally,  $M$  of Fe<sub>4</sub>N has been achieved close to its theoretical values ( $\approx 2.4 \mu_B$ ) in several works [8–11]. Such enhancement in  $M$  with respect to pure Fe ( $M$  of Fe = 2.2  $\mu_B$ ) make them very useful in various applications, e.g., spintronics, magnetic data storage devices [12], permanent magnets, spin-injection electrodes [5], etc. In addition, recent density functional theory calculation

suggests that the SPR for Fe<sub>4</sub>X ( $X = B, C, N$ ) comes out to be 84%, 88%, and 61%, respectively [6].

Furthermore, Fe<sub>4</sub>C is thermally more stable than others (e.g., Fe<sub>4</sub>N or Fe<sub>4</sub>B) due to smaller Fe–C bond distance [4,6,13–15]. Theoretical calculation suggests that Fe–C bond length at 1.8739 Å is smaller as compared to Fe–B (1.9027 Å) or Fe–N (1.8899 Å) [6]. Likewise, other transition metal carbides also show higher thermal stability than nitrides of similar composition. Their thermal stability can also be expressed in terms of Debye-temperature ( $\theta_B$ ), which is a classical limit of the quantum model of Einstein-Debye specific heat for solids. Guillermit *et al.* [16,17] calculated  $\theta_B$  for some transition metal carbides and nitrides and found that in general,  $\theta_B$  of carbides are higher than that of nitrides.

In spite of very interesting magnetic properties, higher SPR and thermal stability, experimental reports on Fe<sub>4</sub>C are almost nonexistent and single-phase Fe<sub>4</sub>C has not yet been synthesized. Recently, interatomic potential for Fe–C systems were calculated using modified embedded atom method (MEAM) and it was predicted that the presence of C lowers the body center cubic (bcc) to face center cubic (fcc) transformation barrier [18,19]. Also the activation energy for C diffusion in Fe was calculated and found to be very small at about 0.8 eV [20]. Both, the reduction in barrier for bcc to fcc and low activation energy point towards favorable conditions for Fe<sub>4</sub>C phase formation. However, the enthalpy of formation ( $\Delta H_f^\circ$ ) for Fe<sub>4</sub>C is positive (about 0.1 eV [6,21]). It may be noted that  $\Delta H_f^\circ$  for early transition metal nitrides and carbides

\*mgupta@csr.res.in

is quite less, e.g.,  $\Delta H_f^\circ = -1.9$  eV for TiC and  $-3.5$  eV for TiN [16]. Therefore synthesis of these compounds take place straight away using standard methods. Even with a slight negative  $\Delta H_f^\circ = -0.15$  eV [4,6], single-phase Fe<sub>4</sub>N has been reported in several works [2]. However, for Fe<sub>4</sub>C, a positive value of  $\Delta H_f^\circ$  leads to a thermodynamically unfavorable condition that can not be achieved utilizing equilibrium processes, e.g., Fischer-Tropsch synthesis (FTS). Recently, FTS was used to synthesize iron carbide (Fe-C) compounds and resulting phases were identified as  $\theta$ -Fe<sub>3</sub>C and  $\chi$ -Fe<sub>5</sub>C<sub>2</sub> from x-ray diffraction and Mössbauer spectroscopy measurements [21].

However, using nonequilibrium processes that are typically found in physical vapor depositions (PVD) methods, formation of Fe<sub>4</sub>C may be feasible. It may be noted that  $\Delta H_f^\circ$  of Fe<sub>16</sub>N<sub>2</sub> is also positive at about 0.88 eV/atom [22]. Using various thin film deposition techniques like e-beam evaporation, molecular beam epitaxy and sputtering, (partial) formation of Fe<sub>16</sub>N<sub>2</sub> has been reported [23,24]. Therefore formation of Fe<sub>4</sub>C may also take place using such nonequilibrium processes. Among PVD methods, co-sputtering is most convenient and effective to synthesize Fe-C compounds as (i) the control of composition can be made precisely by varying the power of each sputter source, (ii) in a confocal geometry, sputtered species from each source mix before depositing on to a substrate, and (iii) adatom energies in sputtering are much higher (typically 10 eV) than that of thermal evaporation (0.1–0.2 eV) [25]. Thus nonequilibrium nature and higher energetics of the depositing species in sputtering have risen a possibility to prepare Fe<sub>4</sub>C.

Some attempts have been made to synthesize Fe-C thin films by sputtering of a compound [Fe + C] target [26–31], or sputtering of Fe using a mixture of Ar + CH<sub>4</sub> [32] or Ar + C<sub>2</sub>H<sub>2</sub> [33]. Utilization of compound target may not be useful to control the composition of Fe-C films and using gases like CH<sub>4</sub> and C<sub>2</sub>H<sub>2</sub> may also result in formation of undesired C-H bonds. On the other hand, co-sputtering of Fe and C from two different sources is a clean method providing a wide range of option to control the composition by changing the flux of each source as demonstrated recently by Furlan *et al.* [34]. A survey of available literature suggests that most of the Fe-C thin films reported hitherto are either amorphous or nanocrystalline. For example, Jouanny *et al.* [32] prepared Fe-C thin films by sputtering of Fe target in Ar/CH<sub>4</sub> gas environment at  $T_s = 373$  K and identified phases were  $\epsilon$ -Fe<sub>3</sub>C at lower CH<sub>4</sub> gas flow and amorphous at higher CH<sub>4</sub> gas flow. Tajima *et al.* deposited Fe-C thin films at 623 K by rf magnetron sputtering of a compound target [26] and phases identified were  $\alpha$ -Fe, Fe<sub>3</sub>C, and Fe<sub>5</sub>C<sub>2</sub>. Weck *et al.* [30] deposited Fe-C thin films by ac magnetron sputtering and reactive cathodic arc evaporation of a compound target (12 and 16 at.% C). Resulting films were found to be nanocrystalline bcc-Fe. Subsequently, Babonneau *et al.* [28] deposited Fe<sub>1-x</sub>C<sub>x</sub> ( $0.26 \leq x \leq 0.74$ ) thin films at various substrate temperatures but resulting films were found to be amorphous. Similarly, Mi *et al.* [29] deposited Fe-C thin films by sputtering of a compound target (at room temperature) and also found amorphous Fe-C phases. More recently, Furlan *et al.* [34] deposited Fe-C thin films by co-sputtering of Fe and C from two separate targets (at 300 K) and varied C concentration from 20.8 to 71.8 at.%. It was observed that the resulting Fe-C films were amorphous, irrespective of the amount of C in Fe.

In this work, we synthesized Fe-C thin films by co-sputtering of Fe and C at different substrate temperature ( $T_s$ ) with a nominal composition of Fe<sub>0.8</sub>C<sub>0.2</sub> so as to attempt the first-ever experimental realization of Fe<sub>4</sub>C. Samples were characterized using x-ray diffraction (XRD) for their structure and the surface and magnetic morphology has been obtained from atomic and magnetic force microscopy (AFM, MFM) measurements, respectively. The information about the nature of bonding has been obtained from XANES measurements at C K and Fe L edges. The magnetization of samples was studied using conversion electron Mössbauer spectroscopy (CEMS) and synchrotron-based nuclear resonant scattering (NRS). In addition, from secondary ion mass spectroscopy (SIMS) depth-profiles measurements, Fe self-diffusion was estimated and compared with a pure Fe sample prepared under similar conditions. We found that at low  $T_s$ , the addition of C suppresses Fe diffusion but at high  $T_s$ , it augments. From above mentioned measurements, we found that the room temperature grown Fe<sub>0.8</sub>C<sub>0.2</sub> film was amorphous but at high- $T_s$ , phases formed are crystalline. At the highest  $T_s$  (773 K), predominantly a Fe<sub>3</sub>C phase has been formed but at an intermediate  $T_s$  of 523 K, a clear presence of Fe<sub>4</sub>C (along with Fe<sub>3</sub>C and Fe) can be seen. Observed results demonstrate the possibilities for formation of crystalline Fe-C phases by co-sputtering. The structural and magnetic properties of thus formed Fe-C phases are presented and discussed in this work.

## II. EXPERIMENTAL DETAILS

Fe and C targets were co-sputtered to prepare iron-carbon (Fe-C) thin films. They were deposited at substrate temperature ( $T_s$ ) = 300, 523, and 773 K with nominal stoichiometric composition for Fe<sub>4</sub>C or Fe<sub>0.8</sub>C<sub>0.2</sub>. Their layer structure was: C(5 nm)|<sup>natural</sup>Fe-C(70 nm)|<sup>57</sup>Fe-C(3 nm)|<sup>natural</sup>Fe-C(100 nm)|C(10 nm)|sub.(Si/Quartz). The C concentration was evaluated using (i) the number of monolayer ( $n$ ) per unit area per unit mole:  $n = \text{mass-number}/\text{mass-density}$ , (ii) the thicknesses of Fe and C equivalent to stoichiometric Fe<sub>0.8</sub>C<sub>0.2</sub> is  $n_{\text{Fe}} \times 0.8$  and  $n_{\text{C}} \times 0.2$ , (iii) and the deposition rates for Fe and C have been optimized to achieve thicknesses obtained for Fe<sub>0.8</sub>C<sub>0.2</sub> composition.

The chamber was evacuated down to a base pressure of  $2 \times 10^{-7}$  hPa. Sputtering was carried out using pure Ar (purity 99.9995%) gas at a working pressure of  $3 \times 10^{-3}$  hPa due to gas flow of 20 sccm. In this layer structure, the <sup>natural</sup>Fe-C (hereafter Fe-C) was prepared by co-sputtering of a  $\phi 3$  inch Fe (purity 99.95%) and  $\phi 3$  inch C (purity 99.999%) target at the sputtering power of 100 (2.17 W/cm<sup>2</sup>) and 156 W (3.42 W/cm<sup>2</sup>), respectively. On the other hand, for the <sup>57</sup>Fe-C, the same C target and a  $\phi 1$  inch <sup>57</sup>Fe (enrichment 95.0%, purity 99.95%) target was used and their sputtering powers were kept at 70 (1.55 W/cm<sup>2</sup>) and 11 W (2.17 W/cm<sup>2</sup>), respectively. To prevent Si diffusion from the substrate and surface contamination of samples, a buffer and capping layer of C was always deposited at room temperature prior to or after the deposition of Fe<sub>0.8</sub>C<sub>0.2</sub> film. For better uniformity of the films, substrate holder was rotated at 60 rpm at a distance of about 12 cm from the target. The structural growth of samples was characterized by XRD measurements using Bruker D8 Advance diffractometer equipped with

Cu  $K_\alpha$  x-ray source. The surface morphology and magnetic domain growth of samples was obtained from AFM and MFM measurements (in tapping mode), respectively. During MFM measurements, the cantilever has been lifted up at a height of 50 nm from the surface, to minimize the effect of topography. The electronic structure of the deposited samples have been investigated using Fe  $L$ - and C  $K$ -edge XANES measurements in total electron yield (TEY) mode under UHV conditions at BL-01 beamline [35], Indus-2 synchrotron radiation source, RRCAT, Indore, India. The local structural and magnetic properties have been determined using CEMS and grazing incidence NRS measurements. The angle of incidence during NRS measurements was kept fixed at the critical angle ( $\theta_c$ )  $\approx 0.21^\circ$  and they were performed at P01 beamline [36] of DESY, Petra III synchrotron radiation source at Hamburg, Germany.

In addition, we also deposited reference samples: (i) pure C thin films at  $T_s = 300, 523,$  and  $773$  K and (ii) pure Fe thin film with a  $^{57}\text{Fe}$  marker layer. The process parameters during the growth of these samples were kept similar to those described for  $\text{Fe}_{0.8}\text{C}_{0.2}$  samples. The structure of pure Fe samples was kept as  $^{\text{natural}}\text{Fe}(70 \text{ nm})|^{57}\text{Fe}(3 \text{ nm})|^{\text{natural}}\text{Fe}(100 \text{ nm})| \text{sub.}(\text{Si}/\text{Quartz})$ . They were grown at  $T_s = 300, 523, 648,$  and  $773$  K. In this case, Fe and  $^{57}\text{Fe}$  have sputtered alternatively from two different sources [at  $100 \text{ W}$  ( $2.17 \text{ W}/\text{cm}^2$ )] and the  $^{57}\text{Fe}$  target was prepared by adding  $^{57}\text{Fe}$  foils within the race track area of  $^{\text{natural}}\text{Fe}$  target. SIMS depth profiles from  $\text{Fe}_{0.8}\text{C}_{0.2}$  and Fe samples have been compared to deduce the effect of C addition on Fe self-diffusion at various  $T_s$ .

### III. RESULTS AND DISCUSSION

#### A. Structure and microstructure

Figure 1 shows the XRD pattern of a pure Fe film [reference sample (a1, a2, and a3)] and  $\text{Fe}_{0.8}\text{C}_{0.2}$  thin films (b1, b2, and b3) deposited at  $T_s = 300, 523,$  and  $773$  K. The XRD pattern [Fig. 1(a1)] of Fe thin film deposited at  $T_s = 300$  K shows growth of the film oriented along (200) plane and when the  $T_s$  exceeds 523 K [Figs. 1(a2) and 1(a3)], the (110) plane becomes prominent. Generally, such variations in preferred orientations are not unexpected and have been observed in several cases like TiN [37–39], AlN [40], etc. and have been explained considering alterations in the adatom mobility, stress/strain, and surface energy due to enhanced  $T_s$  [39,40]. As shown later in this work (Sec. III D), the Fe self-diffusion does not increase appreciably on increasing the  $T_s$  (in fact it decreases slightly at 523 K), therefore arguments related to adatom mobility may not be valid for the change observed in the preferred orientation of Fe films. In a recent work, Schönecker *et al.* calculated the thermal surface free energy and stress of iron at different temperatures and found that surface stress for the (001) surface was much smaller than that of (110) surface at low temperature, but at high temperatures, they become similar [41]. The changes observed in the preferred orientation in our Fe films can be understood from this argument. On the other hand, the width of XRD peaks become narrow as  $T_s$  increases. The crystallite size ( $t$ ) has been calculated using Debye Scherrer formula,  $t = 0.96\lambda/\beta\cos\theta$ , where  $\lambda$  is wavelength of the x rays,  $\beta$  is angular full-width half maxima of the Bragg reflection centered at  $2\theta$ . By

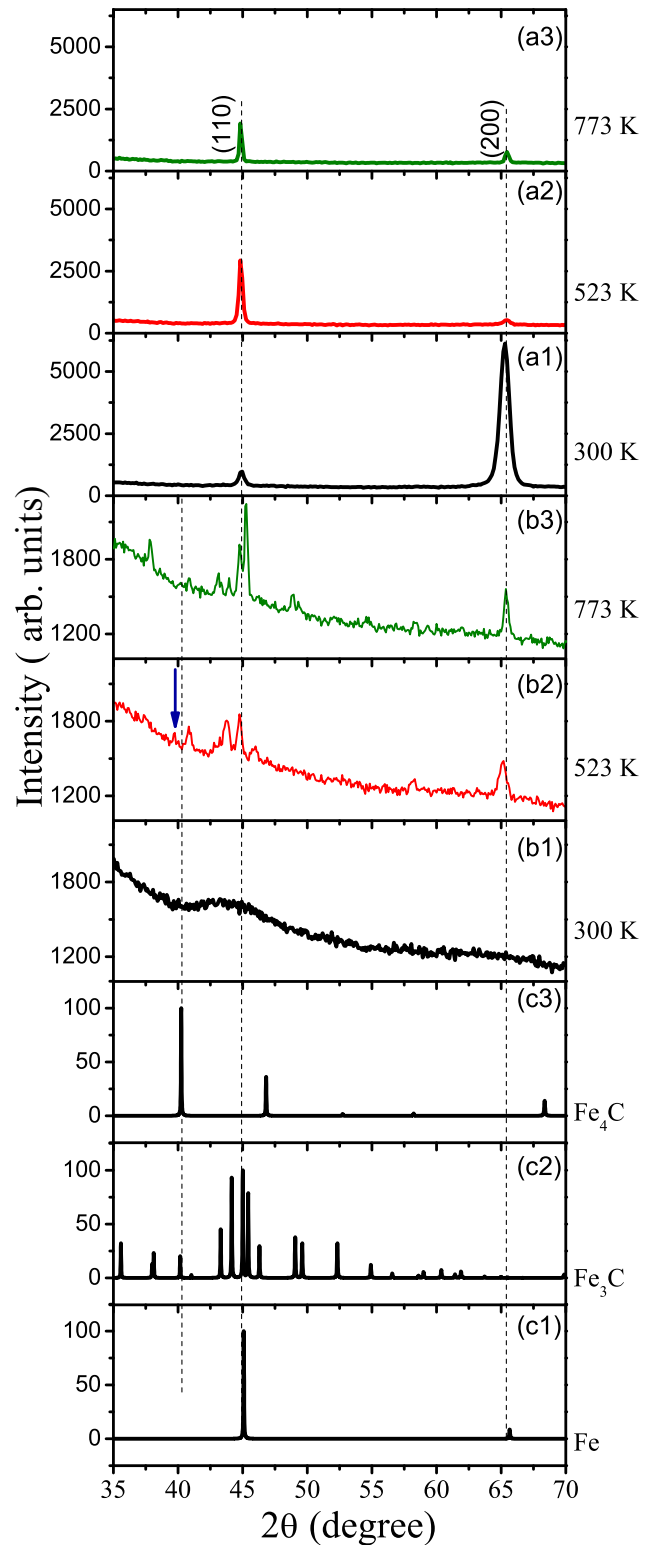


FIG. 1. X-ray diffraction patterns of pure Fe [(a1)–(a3)] and  $\text{Fe}_{0.8}\text{C}_{0.2}$  [(b1)–(b3)] thin films deposited at various substrate temperature. (c1), (c2), and (c3) are the theoretically simulated patterns of Fe,  $\text{Fe}_3\text{C}$ , and  $\text{Fe}_4\text{C}$ , respectively.

increasing the  $T_s$  from 300 to 523 and 773 K,  $t$  increases from  $18 \pm 0.5$  to  $28 \pm 0.5$  and  $46 \pm 2.0$  nm, respectively.

The XRD pattern [Fig. 1(b1)] of the  $\text{Fe}_{0.8}\text{C}_{0.2}$  thin film deposited at  $T_s = 300$  K shows a broad reflection centered

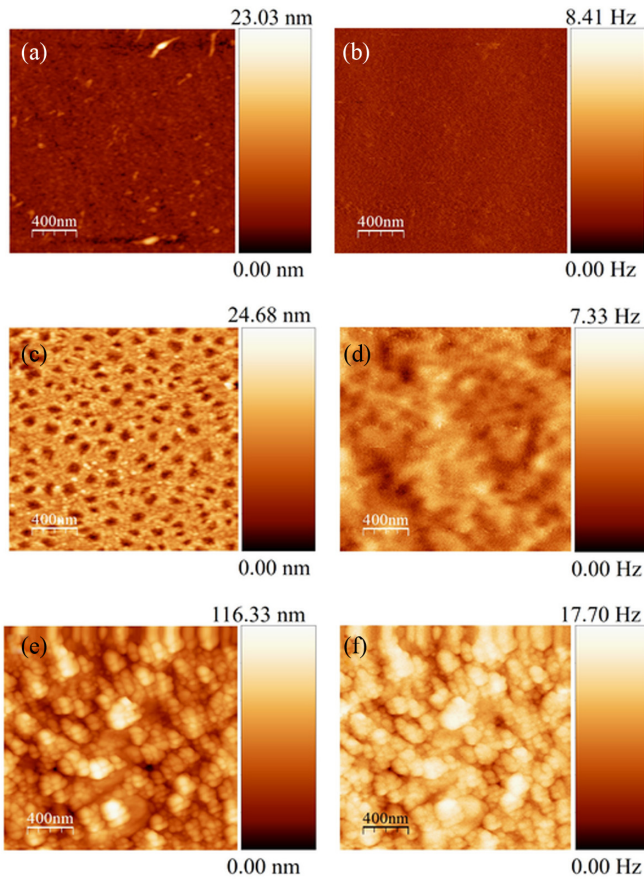


FIG. 2. Atomic force microscopy (AFM) [(a), (c) and (e)], magnetic force microscopy (MFM) [(b), (d), and (f)] images of  $\text{Fe}_{0.8}\text{C}_{0.2}$  samples deposited at 300, 523, and 773 K, respectively, with color scale. The color scale in AFM images represent height and in MFM images it represent cantilever frequency vibrating along  $z$  axis. The  $X \times Y$  scale in all the images are  $2 \times 2 \mu\text{m}$ .

around  $2\theta = (44.58 \pm 0.1)^\circ$  signifying that it has attained an amorphous structure. In an amorphous system, the average nearest-neighbor distance ( $d$ ) can be calculated using:  $d = 1.23\lambda/2 \sin\theta$ , where  $\theta$  is center of the broad reflection and 1.23 is a geometric factor which rationalizes the nearest neighbor distance with the spacing between, “pseudoclose packed planes” [42]. From here, we get  $d = 2.5 \text{ \AA}$ , a value typically found in iron-based amorphous alloys [43]. On the other hand, samples deposited at higher  $T_s$  show a number of peaks. Observed peak positions for the sample deposited at  $T_s = 523$  [Fig. 1(b2)] and 773 K [Fig. 1(b3)] are similar and their intensity is increasing with  $T_s$ . These peak positions are slightly shifted towards lower  $2\theta$  ( $\approx 0.45^\circ$ ) position compared with peak position of theoretically simulated diffraction pattern of  $\theta\text{-Fe}_3\text{C}$  [Fig. 1(c2)] and  $\alpha\text{-Fe}$  [Fig. 1(c1)] phases. Generally, a shift in peak positions are expected due to stress and strain present in thin films. As can be seen in the theoretically simulated XRD pattern of  $\text{Fe}_4\text{C}$  [Fig. 1(c3)] and  $\text{Fe}_3\text{C}$  [Fig. 1(c2)], a faint reflection [marked with an arrow in Fig. 1(b2)] can be attributed to either to  $\text{Fe}_4\text{C}$  or to  $\text{Fe}_3\text{C}$  phases. To clarify this, we prepared another sample with a thicker (10 nm)  $^{57}\text{Fe}\text{-C}$  layer and performed both XRD

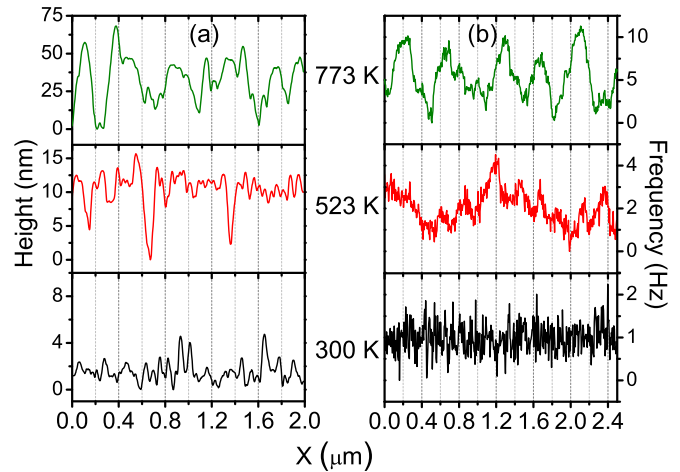


FIG. 3. Height (a) and frequency (b) distribution profiles of atomic force microscopy (AFM) and magnetic force microscopy (MFM) images of the as-deposited  $\text{Fe}_{0.8}\text{C}_{0.2}$  samples, respectively. The profile from AFM is taken along  $x$  axis. In MFM profile, it is taken along the diagonal of the images.

and CEMS measurements that are given in Ref. [44]. From there, it can be unambiguously confirmed that this reflection correspond to  $\text{Fe}_4\text{C}$  phase only. A general observation shows that by increasing  $T_s$ , peak broadening decreases indicating increase in crystallite size. The crystallite size of the evolved phases in the sample deposited at  $T_s = 523$  K comes out to be  $17 \pm 1$  nm of  $\theta\text{-Fe}_3\text{C}$  phase corresponding to (210) reflection centered at  $(43.74 \pm 0.01)^\circ$  and  $26 \pm 1$  nm for  $\alpha\text{-Fe}$  phase corresponding to (110) reflection centered at  $(44.75 \pm 0.01)^\circ$ . Similarly, crystallite size is  $42 \pm 2$  and  $28 \pm 2$  nm for  $\theta\text{-Fe}_3\text{C}$  and  $\alpha\text{-Fe}$  phases, respectively for the sample deposited at  $T_s = 773$  K.

The solubility of C in bcc Fe under ambient condition is very small ( $\approx 0.1$  at.%) [30,45]. Beyond this limit, the presence of C produces a disordered crystal structure due to immiscibility of C with Fe. This results in formation of an amorphous phase in our sample and show agreement with previous reports [34]. Increasing substrate temperature pushes C at the interstitial position of the orthorhombic crystal lattice of Fe, this results in growth of  $\theta\text{-Fe}_3\text{C}$  phase. However, peaks corresponding to unreacted  $\alpha\text{-Fe}$  are also visible.

Figure 2 shows surface and magnetic morphology of the  $\text{Fe}_{0.8}\text{C}_{0.2}$  thin films deposited at various  $T_s$ . Images were processed using WSXM software package [46]. For better understanding of grain and domain growth, we have plotted height and frequency distribution profile of the AFM [Fig. 3(a)] and MFM [Fig. 3(b)] images, respectively. In the AFM image of the sample deposited at  $T_s = 300$  K [Fig. 2(a)], the grains are very small. It is also clear from the height distribution ( $H_d$ ) profile [Fig. 3(a)]. On the other hand, the AFM image of the sample deposited at  $T_s = 523$  K shows enhancement in the grains [Fig. 2(c)] and their  $H_d$  profile shows that they are nearly equal in size. The sample deposited at  $T_s = 773$  K has much larger densely packed grains compared to the other two samples [Fig. 2(e)]. The  $H_d$  profile of the AFM image shows uniform growth of larger grain along with smaller grains. This shows that an increase in  $T_s$  results in formation of larger

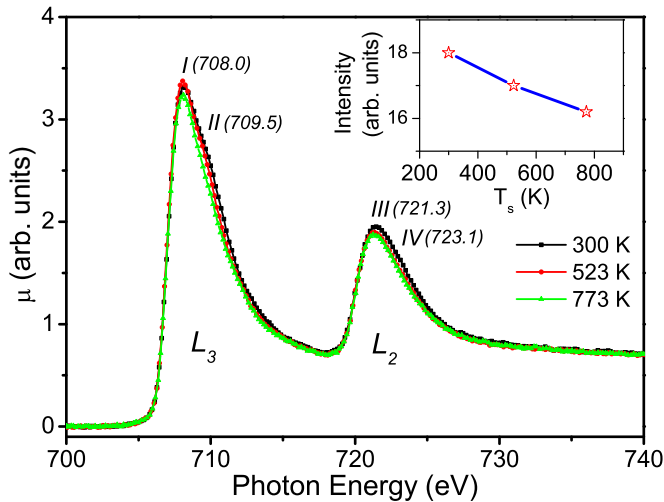


FIG. 4. Fe  $L$ -edge soft x-ray absorption spectra of the  $\text{Fe}_{0.8}\text{C}_{0.2}$  samples deposited at  $T_s = 300, 523,$  and  $773$  K measured in TEY mode. The inset shows variation of integrated intensity with  $T_s$ .

grains. This is in agreement with the XRD results as the grains of  $\theta$ - $\text{Fe}_3\text{C}$  become larger with increase in  $T_s$ .

The MFM images and their frequency distribution profile ( $F_d$ ) show that the sample deposited at  $T_s = 300$  K may have very small magnetic domains [Figs. 2(b) and 3(b)] and they are not clearly visible. The sample deposited at  $T_s = 523$  K have large magnetic domains [Fig. 2(d)] with a systematic change in the cantilever frequency [Fig. 3(b)]. On the other hand, even larger magnetic domains can be seen in the MFM image [Fig. 2(f)] of the sample deposited at  $T_s = 773$  K. However, the magnetic domains are following the pattern similar to topographic changes observed in the AFM [Fig. 2(e)]. In addition, the frequency distribution profile [Fig. 3(b)] shows a change in the frequency similar to change in  $H_d$  profile [Fig. 3(a)]. This is an indication of presence of two kinds of magnetic domain, one with larger and another with smaller size. The MFM image of the sample deposited at  $T_s = 523$  K shows that the structural and magnetic morphologies are different. The  $F_d$  profile shows various frequency maxima with different magnitude [Fig. 3(b)]. This change in the magnetic field of the sample deposited at  $T_s = 523$  K may arise if several magnetic phases are present together. The presence of magnetic phases can be investigated using a local magnetic probe, e.g., Mössbauer spectroscopy based techniques like CEMS and NFS. Results of CEMS and NFS are presented in Sec. III C.

### B. Electronic structure

Local electronic structure was probed using synchrotron based XANES measurements at Fe  $L_{3,2}$  and C  $K$  absorption edges. Figure 4 shows Fe  $L_{3,2}$ -edge XANES spectra of the  $\text{Fe}_{0.8}\text{C}_{0.2}$  thin film deposited at various  $T_s$ , following  $2p \rightarrow 3d$  dipole transition. As indicated, the spectra consist of two prominent transitions occurring due to spin-orbit splitting of  $2p$  orbital in  $L_3$  (I) and  $L_2$  (III) core-shell separated in energy by about 13 eV, which is a typical value for Fe. Each subspectrum further split in double sub-peak due to ligand field splitting marked as II and IV in Fig. 4. Such splitting has

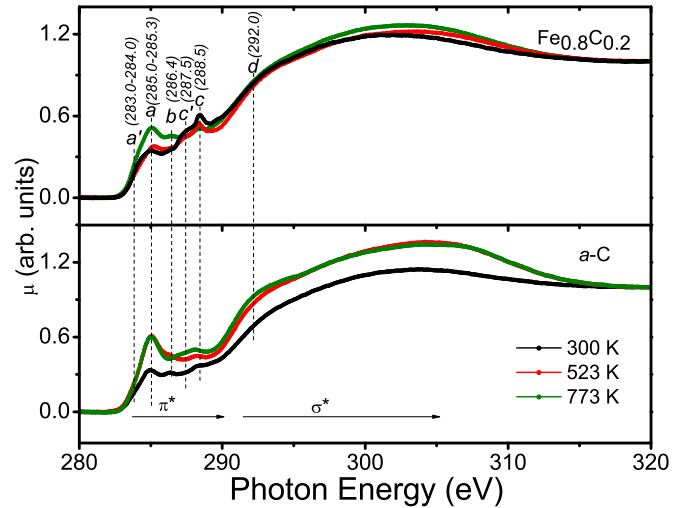


FIG. 5. C  $K$ -edge soft x-ray absorption spectra of the  $\text{Fe}_{0.8}\text{C}_{0.2}$  samples deposited at  $T_s = 300, 523,$  and  $773$  K measured in TEY mode.

been observed in several transition metal-carbides [34,47–49]. The spectra show two characteristic change with  $T_s$  (i) peak become narrow, and (ii) the total integrated intensity of the feature is decreasing as shown in the inset of Fig. 4.

Generally, a narrow Fe  $L_{3,2}$  absorption lines for pure Fe are observed [34]. But, addition of smaller atom, e.g., C, N, O produces splitting due to crystal field and results in broadening of the resonance lines [34]. Their intensity is proportional to the unoccupied Fe  $3d$  states. Decreasing intensity indicates a decrease in charge transfer with increasing  $T_s$ , this results in reduced unoccupied Fe  $3d$  state at higher  $T_s$ . Earlier reports on Fe and Cr  $2p$  XANES spectra of the amorphous system have shown that the peak intensity increases with an increase in C concentration [34,49]. A decrease in the unoccupied state show reduced carbide contribution at higher  $T_s$ . These variations of the spectra show, there can be a possibility of presence of C in unhybridized states at higher  $T_s$ . Further insight about the hybridization has been obtained from C  $K$ -edge XANES measurements.

Figure 5 shows C  $K$ -edge XANES spectra of the Fe-C thin film deposited at various  $T_s$ . The prominent features are marked as  $a, b, c,$  and  $d,$  and shoulders of  $a$  and  $c$  as  $a'$  and  $c'$ , respectively. The feature  $a$  is related with empty  $\pi^*$  states, it is a combination of (i)  $sp^2$  and  $sp^1$  hybridized C states, and (ii) Fe  $3d$ -C  $2p$  hybridized states. In addition, the feature  $c$  is also a combination of (i) Fe  $3d$ -C  $2p$  hybridized states, and (ii) C-O bonding states. These two features show opposite trend with  $T_s$ , with an increase in  $T_s$  the intensity of the feature  $a$  increases while the intensity of the feature  $c$  decreases. A comparison of the C  $K$ -edge spectra of the  $\text{Fe}_{0.8}\text{C}_{0.2}$  thin film with  $a$ -C thin film deposited at  $T_s = 300, 523,$  and  $773$  K shows that the feature  $c$  is shifted by 0.4 eV at lower energy side for  $a$ -C thin films. This shows in case of  $\text{Fe}_{0.8}\text{C}_{0.2}$ , the feature  $c$  is strongly related with Fe  $3d$ -C  $2p$  hybridized states. However, decrease in the intensity of this feature shows reduction in carbide contribution as observed in the Fe  $L_{3,2}$ -edge spectra. Consequently, increase in the intensity of the feature  $a$  signifies presence of higher fraction

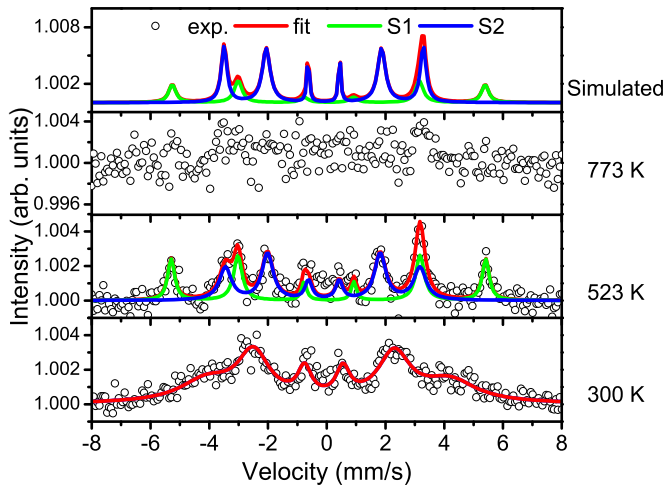


FIG. 6. Conversion electron Mössbauer spectroscopy of the  $\text{Fe}_{0.8}\text{C}_{0.2}$  samples grown at  $T_s = 300, 523,$  and  $773$  K with their respective fit.

of  $sp^2$  hybridized C states at higher  $T_s$ . A shift in the feature  $a$  can be observed at higher energy side by  $0.3$  eV for the sample deposited at  $T_s = 523$  K. This shows that, in addition with reduced carbide contribution at higher  $T_s$ , the sample deposited at  $T_s = 523$  K has different local structure compared to samples deposited at  $T_s = 300$  and  $773$  K. In addition, a faint feature  $b$  is observed at  $286.4$  eV, although the origin of this feature is yet not clear [50].

In addition, the shoulder  $a'$  can be solely due to formation of metal carbide [34,47–49]. The intensity of this shoulder is faint and does not show any significant change. On the other hand, the intensity of the shoulder  $c'$  is decreasing with increase in  $T_s$ . Another report on nanocrystalline TiC/ $a$ -C, shows that the intensity of these features increases with increasing grain sizes as the carbide contribution increases. Unlike TiC/ $a$ -C, decrease in the intensity shows decrease in carbide contribution with increasing  $T_s$ . This shows presence of  $a$ -C in unhybridized state at higher  $T_s$ .

### C. Magnetic structure

Magnetic structure of sandwiched  $3$  nm  $^{57}\text{Fe}$ -C layer was probed using CEMS and NRS measurements. Figure 6 shows experimental CEMS spectra of samples deposited at various  $T_s$  along with fitted data. The CEMS spectrum of the sample deposited at  $300$  K shows broad resonance lines. The broadening of the resonance lines can be related to lack of long-range ordering arisen due to immiscibility of C [51–53]. This spectrum was fitted using one sextet with a hyperfine field ( $B_{\text{hf}}$ ) of  $25.65 \pm 0.34$  T. A  $B_{\text{hf}} = 26$ – $30$  T depending on C content can be observed in amorphous Fe-C alloys [54,55]. This also in a way confirms the amorphous nature of the sample deposited at  $T_s = 300$  K. In comparison to this, the spectrum of the sample deposited at  $T_s = 523$  K shows narrow resonance lines. It was fitted assuming two sextets S1 and S2 with their  $B_{\text{hf}} = 33.20 \pm 0.08$  and  $20.51 \pm 0.13$  T, respectively. Where, S1 and S2 can be assigned to  $\alpha$ -Fe ( $57\%$ ) and  $\theta$ - $\text{Fe}_3\text{C}$  ( $43\%$ ) phases, respectively [21].

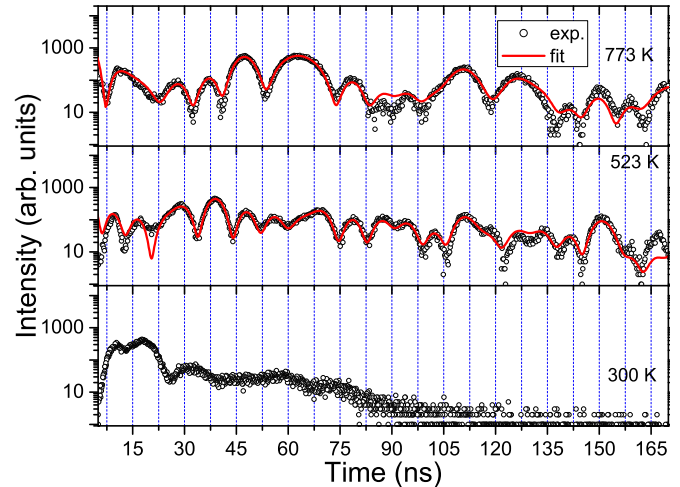


FIG. 7. Nuclear resonant scattering spectra of the  $\text{Fe}_{0.8}\text{C}_{0.2}$  samples deposited  $300, 523,$  and  $773$  K measured at grazing incidence of  $0.21^\circ$  at P01 PETRA III, Germany.

On the other hand, the CEMS spectrum of the sample deposited at  $T_s = 773$  K does not show any prominent resonance even after long counting time (one week). The active % of Mössbauer signal was already low at about  $0.5\%$  due to ultrathin  $^{57}\text{Fe}$ -C layer ( $3$  nm) but at higher  $T_s$  ( $773$  K) the  $^{57}\text{Fe}$ -C layer gets diffused across the entire depth of sample (shown later from SIMS depth profiles), active percentile of Mössbauer signal will reduce further. It may be noted that the mean escape depth of electrons in CEMS is ( $\approx 80$  nm) [56] which is shorter than the total thickness of sample. However, the escape depth of electron also depends on the porous microstructure of the sample [56]. As discussed in Sec. III A, the microstructure of sample deposited at  $773$  K is densely packed compared to other two samples. Thus, the large spread of  $^{57}\text{Fe}$  with  $T_s$  and densely packed microstructure reduces the effective number of resonating nuclei within the escape depth of electron leading to poor statistics. Therefore ensuing magnetic phases, which can be observed in MFM measurements, could not be resolved from CEMS measurement. Such experimental limitation can be overcome by doing synchrotron radiation based NRS measurements.

NRS is a Fourier transform of Mössbauer spectroscopy. This technique is very sensitive to spatial phase factors due to coherent scattering of radiation with matter. It gives a possibility to correlate internal fields with the spatial arrangement of the atoms [57]. Now a days, the availability of enormous brilliance of the synchrotron radiation sources have made it possible to perform such kind of measurements. This technique is frequently used to investigate magnetic properties and phase transitions under high pressure/temperature of nanostructure, ultrathin films, clusters [36], and diffusion in the layered systems [58].

NRS spectra of the  $\text{Fe}_{0.8}\text{C}_{0.2}$  samples deposited at various  $T_s$  are shown in Fig. 7. The spectrum of the sample deposited at  $T_s = 300$  K shows few quantum beats (QBs) with a period of about  $15$  ns confirming the magnetic nature of this sample in accordance with CEMS results [53]. However, the NRS signal decays soon after  $40$  ns which can be understood

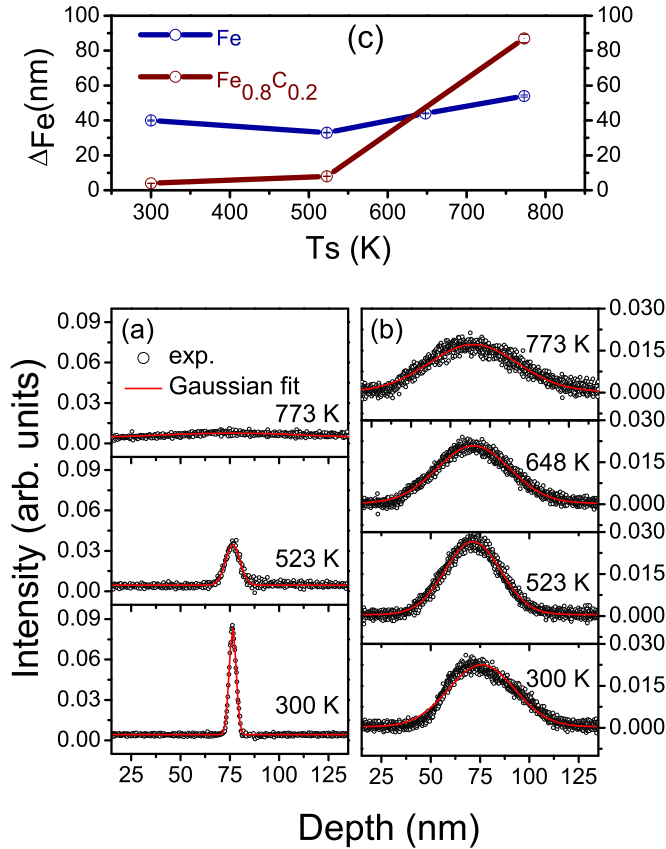


FIG. 8.  $^{57}\text{Fe}$  SIMS concentration profile of samples deposited at different substrate temperature for  $\text{Fe}_{0.8}\text{C}_{0.2}$  films (a) and that of pure Fe films (b). Obtained  $^{57}\text{Fe}$  peak width ( $\Delta_{\text{Fe}}$ ) of these samples are compared in (c).

due to disordered local structure present in the amorphous phase [53]. The NRS signal lasts much longer times ( $>165$  ns) in samples deposited at higher  $T_s$ . The QB period of 523 K sample varies from 5 to 15 ns. On the other hand, it varies from 10 to 15 ns for the sample deposited at 773 K. The smaller QB period reveals presence of a high magnetic moment phase at 523 K. To get more detail information, we fitted NRS spectra of samples deposited at high  $T_s$  using REFTIM software package [59]. The spectrum of the sample deposited at  $T_s = 523$  K can be best fitted using a combination of three hyperfine fields,  $B_{\text{hf}} = 21, 33, 34.3$  T. As already discussed,  $B_{\text{hf}} = 21$  and 33 T are respectively related to  $\theta\text{-Fe}_3\text{C}$  and  $\alpha\text{-Fe}$ , the additional component with larger  $B_{\text{hf}} = 34.3$  T can be assigned to  $\text{Fe}_4\text{C}$  [21] phase only. Their relative volume fractions come out to be 45% for  $\theta\text{-Fe}_3\text{C}$ , 35% for  $\alpha\text{-Fe}$ , and 20% for  $\text{Fe}_4\text{C}$ . On the other hand, the spectrum of the sample deposited at  $T_s = 773$  K can be best fitted assuming two components with  $B_{\text{hf}} = 21$  and 33 T and their relative volume fractions are 70% and 30%, respectively. The absence of  $B_{\text{hf}} = 34.5$  T shows that higher  $T_s$  (773 K) is not favorable for the growth of  $\text{Fe}_4\text{C}$  phase.

#### D. Depth profiling and Fe self-diffusion measurements

Figures 8(a) and 8(b) show SIMS depth profiles of  $\text{Fe}_{0.8}\text{C}_{0.2}$  and pure Fe samples deposited at different  $T_s$ . The

sandwiched  $^{57}\text{Fe}$  layer in both sets of samples results in a peak and it becomes broadened with an increase in  $T_s$ . In  $\text{Fe}_{0.8}\text{C}_{0.2}$  samples  $^{57}\text{Fe}$  peak width ( $\Delta_{\text{Fe}}$ ) is about 4 and 8 nm at  $T_s = 300$  and 523 K, respectively and at  $T_s = 773$  K it has completely diffused throughout the film. On the other hand,  $^{57}\text{Fe}$  profile in pure Fe is significantly broader already at 300 K but the broadening does not increase as much as in Fe-C at higher  $T_s$ . In addition, C concentration has also been estimated from SIMS depth profiles (not shown) and it comes out to be 20, 17, and 13 at.% in samples deposited at  $T_s = 300, 523,$  and 773 K, respectively. This shows C content decreases significantly for the sample deposited at  $T_s = 773$  K. In accordance with XANES spectra, a decrease in C content with  $T_s$  shows that C is moving out from the bulk of the sample.

As can be seen in Fig. 8(a), the trailing side of SIMS profiles are broader than the rising side. Such broadening is observed due to the involvement of sputtering and small intermixing produced by 3 keV  $\text{O}^+$  ions. Such profiles can be corrected using the following equation [60–62]:

$$c_c(x+h) = c_e(x) + h \frac{dc_e(x)}{dx}, \quad (1)$$

where  $c_c$  is corrected and  $c_e$  is experimentally measured concentration profiles and  $h$  is a parameter representing the strength of intermixing. The value of  $h$  was kept constant for a series of samples.

To determine diffusion that is taking place during the growth of our samples, the shape of the tracer profile can be represented as a function of depth ( $x$ ) as

$$c_c(x,t) = \frac{c}{2\sqrt{2Dt}} \exp[-(x^2/4tD(t))], \quad (2)$$

where  $c$  is a constant,  $t$  is annealing time, and  $D$  is diffusion coefficient. Therefore profiles can be fitted using a Gaussian function and diffusion coefficient can be calculated using the following equation [61,62]:

$$\langle D \rangle(t) = \frac{\sigma_t^2 - \sigma_0^2}{2t}, \quad (3)$$

where  $\langle D \rangle(t) = (1/t) \int_0^t D(t') dt'$  is time average diffusion coefficient and  $\sigma_t$  is the standard deviation of Gaussian depth profile over an annealing time of  $t$  or when  $t = 0$ .

Obtained  $\Delta_{\text{Fe}}$  in  $\text{Fe}_{0.8}\text{C}_{0.2}$  and Fe samples are compared in Fig. 8(c). As can be seen that  $\Delta_{\text{Fe}}$  is about 10 times smaller in  $\text{Fe}_{0.8}\text{C}_{0.2}$  as compared to Fe sample deposited at  $T_s = 300$  K. Such a large variation in  $\Delta_{\text{Fe}}$  is somewhat puzzling and unexpected. It is known that fast grain boundary ( $gb$ ) diffusion takes place in Fe due to defects or voids that are incorporated during the growth. The addition of C seems to suppress them significantly. Generally, it is anticipated that  $gb$  diffusion would take place at moderate temperatures. In our case, the information about Fe self-diffusion during growth is obtained, it is new and unique information and can be suitably used to understand the growth of Fe based thin films and also C can be used as an effective dopant to suppress Fe diffusion.

As we increase the  $T_s$ ,  $\Delta_{\text{Fe}}$  increases albeit a small drop in pure Fe deposited at  $T_s = 523$  K. Such a drop-in  $\Delta_{\text{Fe}}$  can be due to an interface sharpening effect that happens due to the release of defects and voids. Such interface sharpening was also evidenced recently in Fe thin films grown at 573 K [63]

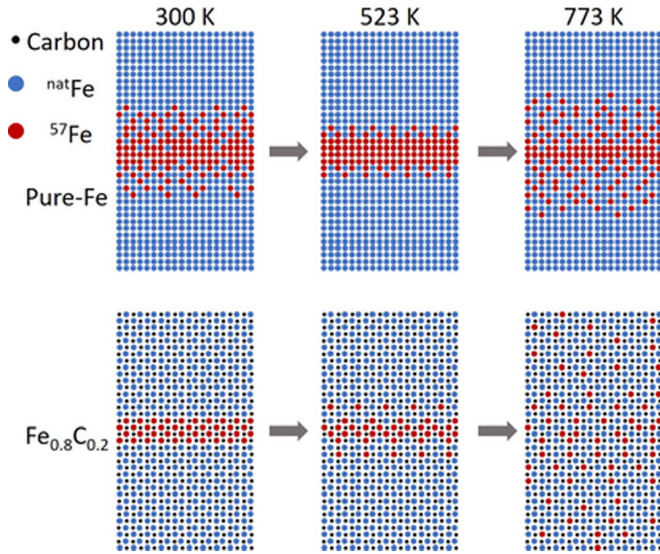


FIG. 9. Schematic representation of diffusion process taking place during growth of  $\text{Fe}_{0.8}\text{C}_{0.2}$  and Fe thin films deposited at  $T_s = 300, 523,$  and  $773$  K.

and also observed in earlier works [64–67]. At  $T_s = 523$  K,  $\Delta_{\text{Fe}}$  in  $\text{Fe}_{0.8}\text{C}_{0.2}$  sample is still significantly smaller as compared to Fe but when samples were grown at  $T_s = 773$  K, a sudden rise in  $\Delta_{\text{Fe}}$  can be seen in  $\text{Fe}_{0.8}\text{C}_{0.2}$  sample. It appears that at low  $T_s$  the presence of C suppress Fe self-diffusion but when the  $T_s$  increases beyond a particular value, Fe diffusion gets augmented. Such kinetics of Fe self-diffusion affects formation of Fe-C phases and will be discussed later. The schematic representation of diffusion process is shown in Fig. 9.

Using the values of  $\Delta_{\text{Fe}}$  in Fe-C and Fe samples grown at  $T_s = 773$  K, we estimated Fe self-diffusion and it comes out to be about an order of magnitude faster in  $\text{Fe}_{0.8}\text{C}_{0.2}$  as compared to Fe ( $6 \pm 1 \times 10^{-19}$   $\text{m}^2/\text{s}$  in Fe-C and  $7 \pm 3 \times 10^{-20}$   $\text{m}^2/\text{s}$  in Fe). Fe self-diffusion coefficient obtained in our sample is close to the value found in earlier works [68–70].

### E. Phase transformation mechanism

From the results obtained in this work, a phase transformation mechanism can be drawn to understand the formation of Fe-C phases during the co-sputtering process. In the co-sputtering process, two or more targets are sputtered simultaneously [here  $\alpha$ -Fe (bcc) and graphite C targets]. The mixing of sputtered Fe and C adatoms takes place when they are still in the vapor phase. In the sputtering process typically, the adatom energy is about 10 eV and as adatom condense on a substrate they lose this energy in picosecond time yielding quenching rates of the order of  $10^{16}$  K/s [71]. These rates are about 10 orders of magnitude higher as compared to melt roller quenching [71]. Generally, with such a high quenching rates, the resulting phase should become amorphous but this is certainly not the case as metallic samples produced by sputtering do possess a long-range ordering. This can be amply seen from the XRD patterns of pure Fe films shown in Fig. 1. Films grown at 300 K are poly crystalline with an average grain size of  $18 \pm 0.5$  nm and with an increase in  $T_s$ ,

the grain size increases to  $28 \pm 0.5$  nm at 523 K,  $45 \pm 1.5$  nm at 648 K, and  $46 \pm 2$  nm at 773 K. This clearly indicates that after condensation on a substrate, the adatom mobility driven diffusion process results in formation of long range ordering and with an increase in  $T_s$ , it increases. As such this is trivial information which is well-known for the growth of thin films with sputtering [72,73]. However, this will be useful to understand the role of C in affecting phase formation in Fe-C thin films.

Aforementioned, we placed a 3-nm  $^{57}\text{Fe}$  marker layer between natural Fe layers, and through this, we could measure Fe self-diffusion that is taking place during the growth of film. We found that already at 300 K, the broadening in  $^{57}\text{Fe}$  profile,  $\Delta_{\text{Fe}}$  is quite large at about 40 nm which is more than ten times the thickness of the marker layer. However, with an increase in  $T_s$ ,  $\Delta_{\text{Fe}}$  does not increase as much. Therefore it appears that Fe self-diffusion takes place rapidly during the initial stages of growth and thereafter it reduces significantly. Fu *et al.* [74] did multiscale modeling of defect kinetics in iron and found that the activation energy ( $E$ ) for interstitial migration can be as low as 0.3 eV in  $\alpha$ -Fe. In an experimental study on Fe self-diffusion in Fe/ $^{57}\text{Fe}$  multilayers, it was also found  $E$  was small ( $E \ll 1$  eV) and has been explained in terms of structural defects in Fe that lead to fast Fe diffusion during initial stages which subsequently becomes smaller when defects relaxation process gets completed [75]. In a recent study also, fast Fe diffusion has been observed and explains in terms of triple junctions leading to short-circuit diffusion [63]. In a way, the fast Fe diffusion during initial stages can be understood as grain boundary ( $gb$ ) diffusion. When the  $gb$  diffusion gets over, the annihilation of defect causes Fe atoms to diffuse through a classical volume type diffusion via thermal vacancies with very high  $E \approx 3$  eV.

The addition of C in Fe affects the  $gb$  diffusion process, so much that  $\Delta_{\text{Fe}} \rightarrow 0$ . Instead of 40 nm for Fe, the  $\Delta_{\text{Fe}}$  in Fe-C was about 4 nm, close to its nominal thickness of 3 nm. And within experimental accuracy, it can be inferred that  $\Delta_{\text{Fe}} \approx 0$  in Fe-C as compared to pure Fe. In this scenario, C atoms restrict the path of Fe atoms thereby leading to the formation of an amorphous structure as observed in our Fe-C samples and also in previous studies [28,29,34]. However, when  $T_s$  increases to 773 K even more rapid Fe diffusion takes place, compared to the case when C was not added as shown in Fig. 8(c). Such an enhancement clearly indicates that in presence of C, the concentration of defects may become even higher leading to faster Fe diffusion through  $gb$ . But at an intermediate temperature of 523 K, we found that Fe diffusion was still low and crystalline Fe-C phases like  $\text{Fe}_3\text{C}$  and  $\text{Fe}_4\text{C}$  start to nucleate. And at this temperature regime, it seems that kinetics of Fe-C phase formation is driven by C diffusion. Recently, it has been revealed in a computational ReaxFF study (based on bond order concept [76]) that C diffuses through  $gb$  [20] and  $E$  for C diffusion is typically about 0.8 eV. Also, as suggested by theoretical calculations, the energy barrier for  $\alpha$  (bcc)  $\rightarrow$   $\gamma$  (fcc) phase transformation of Fe is about 0.137 eV/atom but it gets reduced to 0.127 eV/atom in presence of C [18,19]. On the other hand, for the reverse case, i.e.,  $\gamma \rightarrow \alpha$  phase it is much smaller at about 0.025 eV/atom for Fe but it increases marginally to 0.047 eV/atom for Fe-C. The presence of C in Fe lattice produces local stress



field, resulting enhancement in the energy barrier for  $\gamma \rightarrow \alpha$  [18,19]. Therefore the presence of C prevents  $\gamma \rightarrow \alpha$  and favors the  $\alpha \rightarrow \gamma$  phase transformation. These conditions are suitably met at the intermediate temperature of 523 K and by further fine tuning the amount of C and  $T_s$  around 523 K, it may be possible increase the fraction of  $\text{Fe}_4\text{C}$  phase or even a single phase  $\text{Fe}_4\text{C}$  phase can be obtained.

#### IV. CONCLUSION

In conclusion, in the present work, we systematically studied the role of substrate temperature and phase formation in Fe-C thin films around  $\text{Fe}_{0.8}\text{C}_{0.2}$  composition. A comparison of  $\text{Fe}_{0.8}\text{C}_{0.2}$  films together with pure Fe films (grown under similar conditions) exhibited the effect of C inclusion on the long-range crystalline ordering. In addition, the comparison of  $\text{Fe}_{0.8}\text{C}_{0.2}$  films with C thin films yielded vital information about the hybridization between Fe and C. By inserting a thin  $^{57}\text{Fe}$  or  $^{57}\text{Fe}_{0.8}\text{C}_{0.2}$  marker layer in between thick Fe or  $\text{Fe}_{0.8}\text{C}_{0.2}$  layers, Fe self-diffusion that is taking place during the growth itself was measured. We found Fe self-diffusion was appreciably large even at 300 K, but the addition of C in Fe inhibits Fe self-diffusion remarkably. At the high  $T_s$

of 773 K, C addition leads to very rapid Fe self-diffusion. However, at an intermediate temperature of  $T_s$  of 523 K, Fe self-diffusion is still low and controllable so that formation of  $\text{Fe}_4\text{C}$  phase could be realized. It can be anticipated that by further fine tuning of  $T_s$  and C composition, the fraction of  $\text{Fe}_4\text{C}$  can be further enhanced. The information about such Fe diffusion process in Fe-C system is new and can be suitably used to synthesize challenging Fe-C phases.

#### ACKNOWLEDGMENTS

Authors would like to acknowledge Layanta Behera for technical help, Anil Gome for CEMS, Mohan Gangrade for AFM and MFM, Rakesh Sah for XANES, and Nidhi Pandey for NRS measurements. We are thankful to A. K. Sinha for support and encouragements and Seema for fruitful discussions. Portions of this research were carried out at the light source PETRA III of DESY, a member of the Helmholtz Association (HGF). Financial support by the Department of Science & Technology (Government of India) provided within the framework of the India @ DESY collaboration is gratefully acknowledged.

- 
- [1] S. Matar, P. Mohn, G. Demazeau, and B. Siberchicot, *J. de Phys.* **49**, 1761 (1988).
- [2] E. L. P. y Blancá, J. Desimoni, N. E. Christensen, H. Emmerich, and S. Cottenier, *Physica Status Solidi (b)* **246**, 909 (2009).
- [3] Y. Takahashi, Y. Imai, and T. Kumagai, *J. Mag. Mag. Mater.* **323**, 2941 (2011).
- [4] C.-M. Fang, R. S. Koster, W.-F. Li, and M. A. van Huis, *RSC Adv.* **4**, 7885 (2014).
- [5] S. Kokado, N. Fujima, K. Harigaya, H. Shimizu, and A. Sakuma, *Phys. Rev. B* **73**, 172410 (2006).
- [6] Z. Lv, Y. Gao, S. Sun, M. Qv, Z. Wang, Z. Shi, and W. Fu, *J. Mag. Mag. Mater.* **333**, 39 (2013).
- [7] A. Houari, S. F. Matar, and M. A. Belkhir, *J. Mag. Mag. Mater.* **322**, 658 (2010).
- [8] N. Pandey, S. Pütter, S. M. Amir, V. R. Reddy, D. M. Phase, J. Stahn, A. Gupta, and M. Gupta, *Phys. Rev. Mater.* **3**, 114414 (2019).
- [9] K. Ito, G. H. Lee, K. Harada, M. Suzuno, T. Suemasu, Y. Takeda, Y. Saitoh, M. Ye, A. Kimura, and H. Akinaga, *Appl. Phys. Lett.* **98**, 102507 (2011).
- [10] T. Takahashi, N. Takahashi, N. Tamura, T. Nakamura, M. Yoshioka, W. Inami, and Y. Kawata, *J. Mater. Chem.* **11**, 3154 (2001).
- [11] J. L. Costa-Krämer, D. M. Borsa, J. M. García-Martín, M. S. Martín-González, D. O. Boerma, and F. Briones, *Phys. Rev. B* **69**, 144402 (2004).
- [12] O. Kohmoto, *IEEE Trans. Mag.* **27**, 3640 (1991).
- [13] C. M. Fang, M. A. van Huis, J. Jansen, and H. W. Zandbergen, *Phys. Rev. B* **84**, 094102 (2011).
- [14] C. M. Fang, M. A. van Huis, B. J. Thijssse, and H. W. Zandbergen, *Phys. Rev. B* **85**, 054116 (2012).
- [15] W. Zhang, Z. Lv, Z. Shi, S. Sun, Z. Wang, and W. Fu, *J. Mag. Mag. Mater.* **324**, 2271 (2012).
- [16] A. F. Guillermet and G. Grimvall, *Phys. Rev. B* **40**, 10582 (1989).
- [17] A. Fernández Guillermet, J. Häglund, and G. Grimvall, *Phys. Rev. B* **45**, 11557 (1992).
- [18] T. Q. Nguyen, K. Sato, and Y. Shibusani, *Mater. Trans.* **59**, 870 (2018).
- [19] T. Q. Nguyen, K. Sato, and Y. Shibusani, *Comput. Mater. Sci.* **150**, 510 (2018).
- [20] K. Lu, C.-F. Huo, Y. He, J. Yin, J. Liu, Q. Peng, W.-P. Guo, Y. Yang, Y.-W. Li, and X.-D. Wen, *J. Phys. Chem. C* **122**, 23191 (2018).
- [21] X.-W. Liu, S. Zhao, Y. Meng, Q. Peng, A. K. Dearden, C.-F. Huo, Y. Yang, Y.-W. Li, and X.-D. Wen, *Sci. Rep.* **6**, 26184 (2016).
- [22] F. Tessier, A. Navrotsky, R. Niewa, A. Leineweber, H. Jacobs, S. Kikkawa, M. Takahashi, F. Kanamaru, and F. DiSalvo, *Solid State Sci.* **2**, 457 (2000).
- [23] Y. Sugita, H. Takahashi, M. Komuro, M. Igarashi, R. Imura, and T. Kambe, *J. Appl. Phys.* **79**, 5576 (1996).
- [24] M. Takahashi, H. Shoji, H. Takahashi, H. Nashi, T. Wakiyama, M. Doi, and M. Matsui, *J. Appl. Phys.* **76**, 6642 (1994).
- [25] M. Ohring, in *Materials Science of Thin Films*, edited by M. Ohring, 2nd ed. (Academic Press, San Diego, 2002), pp. 145–202.
- [26] S. Tajima and S. Hirano, *J. Mater. Sci.* **28**, 2715 (1993).
- [27] D. Babonneau, T. Cabioçâh, M.-F. Denanot, and A. Naudon, *Appl. Phys. Lett.* **74**, 800 (1999).
- [28] D. Babonneau, J. Briatico, F. Petroff, T. Cabioçâh, and A. Naudon, *J. Appl. Phys.* **87**, 3432 (2000).
- [29] W. B. Mi, Z. Q. Li, P. Wu, E. Y. Jiang, and H. L. Bai, *J. Phys.: Condens. Matter* **16**, 5569 (2004).
- [30] A. Weck, C. W. Sinclair, C. P. Scott, and C. Maunder, *J. Mater. Sci.* **47**, 6939 (2012).
- [31] W. B. Mi, Z. Q. Li, P. Wu, E. Y. Jiang, H. L. Bai, D. L. Hou, and X. L. Li, *J. Appl. Phys.* **97**, 043903 (2005).
- [32] I. Jouanny, V. Demange, J. Ghanbaja, and E. Bauer-Grosse, *J. Mater. Res.* **25**, 1859 (2010).

- [33] A. Kirilyuk, J. Giergiel, J. Shen, M. Straub, and J. Kirschner, *Phys. Rev. B* **54**, 1050 (1996).
- [34] A. Furlan, U. Jansson, J. Lu, L. Hultman, and M. Magnuson, *J. Phys.: Condens. Matter* **27**, 045002 (2015).
- [35] D. M. Phase, M. Gupta, S. Potdar, L. Behera, R. Sah, and A. Gupta, in *Solid State Physics: Proceedings of the 58th DAE Solid State Physics Symposium 2013*, edited by C. Murli, D. Bhattacharyya, and S. C. Gadhari, AIP Proc. No. 1591 (AIP, New York, 2013).
- [36] H.-C. Wille, H. Franz, R. Röhlberger, W. A. Caliebe, and F.-U. Dill, *J. Phys.: Conf. Ser.* **217**, 012008 (2010).
- [37] J.-E. Sundgren, *Thin Solid Films* **128**, 21 (1985).
- [38] U. C. Oh and J. H. Je, *J. Appl. Phys.* **74**, 1692 (1993).
- [39] P. Patsalas, C. Charitidis, and S. Logothetidis, *Surf. Coat. Technol.* **125**, 335 (2000).
- [40] F. Medjani, R. Sanjinés, G. Allidi, and A. Karimi, *Thin Solid Films* **515**, 260 (2006).
- [41] S. Schönecker, X. Li, B. Johansson, S. K. Kwon, and L. Vitos, *Sci. Rep.* **5**, 14860 (2015).
- [42] L. Katz, *J. Chem. Educ.* **41**, 292 (1964).
- [43] M. E. McHenry, M. A. Willard, and D. E. Laughlin, *Prog. Mater. Sci.* **44**, 291 (1999).
- [44] See Supplemental Material at <http://link.aps.org/supplemental/10.1103/PhysRevMaterials.4.013402> for Structural and magnetic properties of Fe-C thin film characterized using x-ray diffraction and Mössbauer spectroscopy measurements.
- [45] W. D. Callister, *Materials Science and Engineering: An Introduction* (Wiley-VCH, 2006).
- [46] I. Horcas, R. Fernández, J. M. Gómez-Rodríguez, J. Colchero, J. Gómez-Herrero, and A. M. Baro, *Rev. Sci. Instrum.* **78**, 013705 (2007).
- [47] M. Magnuson, O. Wilhelmsson, J.-P. Palmquist, U. Jansson, M. Mattesini, S. Li, R. Ahuja, and O. Eriksson, *Phys. Rev. B* **74**, 195108 (2006).
- [48] M. Magnuson, E. Lewin, L. Hultman, and U. Jansson, *Phys. Rev. B* **80**, 235108 (2009).
- [49] M. Magnuson, M. Andersson, J. Lu, L. Hultman, and U. Jansson, *J. Phys.: Condens. Matter* **24**, 225004 (2012).
- [50] P. Kumar, M. Gupta, U. Deshpande, D. Phase, V. Ganesan, and J. Stahn, *Diamond Relat. Mater.* **84**, 71 (2018).
- [51] M. Miglierini and J.-M. Greneche, *J. Phys.: Condens. Matter* **9**, 2303 (1997).
- [52] T. Glaser, *Angew. Chem. Int. Ed.* **50**, 10019 (2011).
- [53] M. Miglierini and P. Matú, *Pure Appl. Chem.* **89**, 405 (2017).
- [54] F. Miani, P. Matteazzi, and D. Basset, *J. Alloys Compd.* **204**, 151 (1994).
- [55] S. Amagasa, N. Nishida, Y. Kobayashi, and Y. Yamada, *Hyperfine Interact.* **237**, 110 (2016).
- [56] F. Moutinho, C. Rojas, and L. D’Onofrio, in *Proceedings of the 11th Latin American Conference on the Applications of the Mössbauer Effect, LACAME 2008*, edited by J. Desimoni, C. Ramos, B. Arcondo, F. D. Saccone, and R. Mercader (Springer, Berlin, Heidelberg, 2009), pp. 141–147.
- [57] R. Röhlberger, *Nuclear Condensed Matter Physics with Synchrotron Radiation* (Springer, Berlin, Heidelberg, 2005).
- [58] A. Gupta, M. Gupta, S. Chakravarty, R. Ruffer, H.-C. Wille, and O. Leupold, *Phys. Rev. B* **72**, 014207 (2005).
- [59] M. A. Andreeva, *Hyperfine Interact.* **185**, 17 (2008).
- [60] G. Brebec, R. Seguin, C. Sella, J. Bevenot, and J. Martin, *Acta Metallurgica* **28**, 327 (1980).
- [61] Y. Loirat, J. Bocquet, and Y. Limoge, *J. Non-Crystalline Solids* **265**, 252 (2000).
- [62] M. Gupta, A. Gupta, S. Rajagopalan, and A. K. Tyagi, *Phys. Rev. B* **65**, 214204 (2002).
- [63] A. Tiwari, M. K. Tiwari, M. Gupta, H.-C. Wille, and A. Gupta, *Phys. Rev. B* **99**, 205413 (2019).
- [64] H. L. Bai, E. Y. Jiang, C. D. Wang, and R. Y. Tian, *J. Phys.: Condens. Matter* **8**, 8763 (1996).
- [65] J. B. Kortright, S. Joksich, and E. Ziegler, *J. Appl. Phys.* **69**, 168 (1991).
- [66] M. Ishino, M. Koike, M. Kanehira, F. Satou, M. Terauchi, and K. Sano, *J. Appl. Phys.* **102**, 023513 (2007).
- [67] S. Amir, M. Gupta, and A. Gupta, *J. Alloys Compd.* **522**, 9 (2012).
- [68] M. Lübbehusen and H. Mehrer, *Acta Metallurgica et Materialia* **38**, 283 (1990).
- [69] Y. Iijima, *J. Phase Equilib. Diffus.* **26**, 466 (2005).
- [70] S. Chakravarty, N. Shukla, A. Devishvili, A. Vorobiev, and G. Amarendra, *Mater. Res. Express* **3**, 085001 (2016).
- [71] K. Wasa, in *Handbook of Sputtering Technology*, edited by K. Wasa, I. Kanno, and H. Kotera, 2nd ed. (William Andrew, Oxford, 2012), pp. xi–xii.
- [72] V. Bhavanasi, C. B. Singh, D. Datta, V. Singh, K. Shahi, and S. Kumar, *Optical Mater.* **35**, 1352 (2013).
- [73] X.-Y. Li, H.-J. Li, Z.-J. Wang, H. Xia, Z.-Y. Xiong, J.-X. Wang, and B.-C. Yang, *Optics Commun.* **282**, 247 (2009).
- [74] C.-C. Fu, J. D. Torre, F. Willaime, J.-L. Bocquet, and A. Barbu, *Nat. Mater.* **4**, 68 (2005).
- [75] S. Chakravarty, H. Schmidt, U. Tietze, D. Lott, N. P. Lalla, and A. Gupta, *Phys. Rev. B* **80**, 014111 (2009).
- [76] A. C. T. van Duin, S. Dasgupta, F. Lorant, and W. A. Goddard, *J. Phys. Chem. A* **105**, 9396 (2001).